|| Volume 9 || Issue 7 || July 2025 || ISSN (Online) 2456-0774
INTERNATIONAL JOURNAL OF ADVANCE SCIENTIFIC RESEARCH
AND ENGINEERING TRENDS

Photoluminescence and Structural Analysis of Eu^{3+}-Doped $Mg_4P_2O_7$ and $Ca_4P_2O_7$ Nanophosphors for Red-Emitting Applications

Roshni Haldkar[1],R.K.Kuraria[2], S.R.Kuraria*[3],Anjali Yadav[4]

[1]*Govt. M.H. College Jabalpur, Madhya Pradesh 482002, India*

[2]*Vice chancellor Awdhesh Pratap Singh University (APSU) Rewa, Madhya Pradesh 486002, India*

[3]*Govt. Science College, Jabalpur(M.P.) 482001, India 4. Govt. Adarsh College Dindori,Madhya Pradesh, 481880, India*

haldkarroshni1992@gmail.com,rkkuraria62@gmail.com

Abstract: This study explores the synthesis, structural characterization, and photoluminescence properties of Eu^{3+} -doped $Mg_4P_2O_7$ and $Ca_4P_2O_7$ nanophosphors. Utilizing glycine-assisted solution combustion and high-temperature solid-state methods, phase-pure and highly crystalline phosphors were developed. Structural features were investigated through X-ray diffraction (XRD), Fourier-transform infrared (FT-IR) spectroscopy, scanning electron microscopy (SEM), and transmission electron microscopy (TEM). The $Mg_4P_2O_7:Eu^{3+}$ phosphor exhibited intense red emission centered at 615 nm under 395 nm excitation, corresponding to the $^5D_0 \rightarrow {}^7F_2$ electric dipole transition. In contrast, $Ca_4P_2O_7$:Eu showed strong blue emission around 422 nm, attributed to the partial reduction of Eu^{3+} to Eu^{2+}. Thermogravimetric analysis (TGA) confirmed excellent thermal stability, supporting the potential of these phosphors in white light-emitting diodes (w-LEDs) and optoelectronic devices.

Keywords: *Europium, $Mg_4P_2O_7$, $Ca_4P_2O_7$, Photoluminescence, Nanophosphors, Red-emitting phosphors*

I.INTRODUCTION:

In recent years, the demand for efficient and stable luminescent materials has surged due to their widespread applications in solid-state lighting, flat-panel displays, bioimaging, security printing, and optoelectronic devices. Among the various classes of luminescent materials, rare-earth (RE)-doped phosphors have gained prominence because of their unique electronic configurations that allow for sharp and intense emission lines, long lifetimes, and high quantum efficiency. Europium ions, in particular, are extensively studied due to their versatile emission capabilities. While Eu^{2+} shows broad-band emission in the blue or green region due to allowed $4f^6\ 5d^1 \rightarrow 4f^7$ transitions, Eu^{3+} exhibits line-like emissions in the red region, primarily due to intra-4f transitions such as $5D_0 \rightarrow 7F_2$**[1-5]**.

The choice of a suitable host lattice is crucial for optimizing the photoluminescent properties of rare-earth ions. Phosphate-based materials, such as pyrophosphates, offer a favorable combination of low phonon energy, high thermal and chemical stability, and structural flexibility, making them ideal matrices for RE doping. Among them, magnesium pyrophosphate ($Mg_4P_2O_7$) and calcium pyrophosphate ($Ca_4P_2O_7$) have emerged as promising hosts due to their robust crystal structures and ability to accommodate RE ions without significant lattice distortion.

The pyrophosphate framework, consisting of two PO_4 tetrahedra sharing an oxygen atom ($P_2O_7^{4-}$), provides a rigid and interconnected network that helps suppress non-radiative relaxation processes, thereby enhancing luminescence**[6-10]**.

Despite the potential of $Mg_4P_2O_7$ and $Ca_4P_2O_7$ as host materials, comprehensive studies comparing their structural and optical behavior when doped with Eu^{3+} are limited. This study aims to synthesize and compare Eu^{3+}-doped $Mg_4P_2O_7$ and $Ca_4P_2O_7$ nanophosphors, focusing on their phase formation, morphological features, thermal behavior, and photoluminescent performance. The red emission from Eu^{3+} and potential blue emission from in-situ reduced Eu^{2+} under UV excitation are investigated for their suitability in white light-emitting diode (w-LED) applications.

II.EXPERIMENTAL SECTION

2.1 Material and Synthesis

Analytical grade magnesium nitrate, calcium nitrate, ammonium dihydrogen phosphate, europium nitrate, and glycine were used without further purification. The phosphors were synthesized via a glycine-assisted solution combustion method. In a typical process, stoichiometric amounts of metal nitrates and phosphate sources were dissolved in deionized water. Glycine, serving as both fuel and complexing agent, was added in excess. The resulting gel was heated at 80–90 °C until a viscous precursor formed. This precursor was calcined in a muffle furnace at 500–600 °C to trigger combustion, followed by annealing at 900–1100 °C for improved crystallinity.

2.2 Characterization Techniques

XRD analysis was carried out to identify phase formation and crystallinity. FT-IR spectroscopy confirmed phosphate functional groups. SEM and TEM provided morphological insights at micro and nanoscale levels. TGA was performed to assess thermal decomposition behavior. Photoluminescence spectra were recorded at room temperature using a spectrofluorometer equipped with a xenon lamp**[11-20]**.

III.RESULT AND DISCUSSION

3.1 Structural Analysis (XRD)

The phase purity and crystalline structure of the synthesized $Mg_4P_2O_7$:Eu_x phosphor samples were examined using powder X-ray diffraction (XRD) with Cu Kα radiation (λ = 1.5406 Å). The recorded diffraction pattern exhibits a series of sharp and well-defined peaks, indicating the crystalline nature of the phosphor. The experimental pattern (shown in blue) matches closely with the calculated reference pattern (shown in red), confirming the successful formation of a single-phase orthorhombic structure corresponding to magnesium pyrophosphate ($Mg_4P_2O_7$).

The most intense diffraction peak was observed at 2θ ≈ 30.5°, indexed to the (211) plane, suggesting a preferred orientation along this direction. Other characteristic peaks appeared at 2θ values corresponding to the planes (110), (101), (200), (111), (210), (201), (310), (301), (212), (410), (402), (222), (330), (411), (312), and so on, matching well with the standard JCPDS file of $Mg_4P_2O_7$. The close agreement between the experimental and calculated peak positions and intensities, along with the low residual value (Rp = 18.3%), supports the high crystallinity and phase purity of the synthesized material.For the Eu^{3+}-doped sample, the crystallite size was estimated to be 40.1 nm.

Notably, no secondary or impurity phases were detected in the XRD pattern, indicating that the doping of Eu^{3+} ions into the $Mg_4P_2O_7$ lattice did not significantly alter the host crystal structure. The absence of peak shifting also suggests that the Eu^{3+} ions were successfully incorporated into the lattice at low concentrations without inducing significant lattice distortion. This structural integrity is crucial for ensuring consistent luminescence performance in phosphor materials. The XRD analysis confirms the successful synthesis of phase-pure, crystalline Eu^{3+}-doped $Mg_4P_2O_7$, suitable for further investigation of its photoluminescence properties.

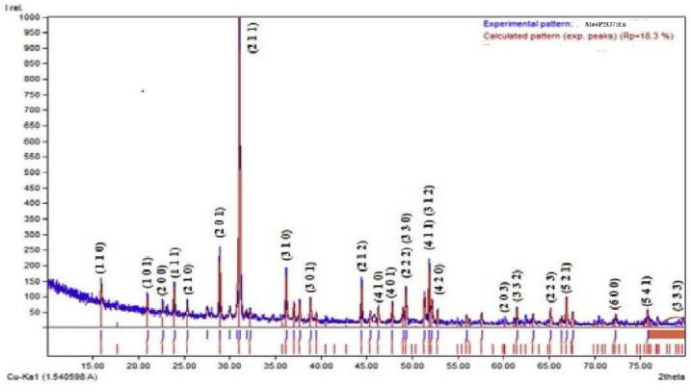

Figure 1: XRD of $Mg_4P_2O_7$:Eu_x

To examine the crystallographic structure and phase purity of the synthesized $Ca_4P_2O_7$:x% Eu^{3+} phosphors, XRD measurements were conducted on samples calcined at various temperatures ranging from 900°C to 1100°C. The XRD patterns are shown in Figure (above), and all diffraction peaks are in close agreement with the standard diffraction data of $Ca_4P_2O_7$ (PDF #01-071-2123), indicating successful formation of the target phase. No significant secondary phases were detected at lower temperatures, suggesting that the Eu^{3+} dopant was successfully incorporated into the $Ca_4P_2O_7$ lattice without inducing structural degradation or unwanted side products.

As the calcination temperature increased, the diffraction peaks became progressively sharper and more intense, indicating enhanced crystallinity and grain growth. At 900°C, the peaks appear broad and relatively weak, reflecting partial crystallization and possibly the presence of some amorphous content. Upon increasing the temperature to 950°C and 1000°C, the peak intensities improve, and the patterns begin to closely match the reference pattern. Notably, at 1050°C and 1100°C, the XRD peaks become distinctly sharp and well-resolved, indicating the formation of a highly crystalline and pure $Ca_4P_2O_7$ phase. The peaks at around 2θ ≈ 29.5°, 30.5°, and 31.2° are particularly prominent and match well with the reference diffraction lines of the standard phase.For the Eu^{3+}-doped sample, the crystallite size was estimated to be 40.1 nm.

A magnified view in the 2θ range of 29–33° clearly shows a slight shift in peak positions and intensity variation with temperature, which may be attributed to the gradual incorporation of Eu^{3+} ions into the Ca^{2+} lattice sites and the resulting slight lattice distortion due to the difference in ionic radii. The presence of a minor secondary peak marked with a diamond symbol (♦) at higher temperatures may suggest a trace amount of secondary phase formation (possibly due to Eu-rich regions or local phase segregation), but this does not significantly affect the overall structural purity.

Overall, the XRD analysis confirms that the $Ca_4P_2O_7$ host lattice maintains its monoclinic phase structure upon Eu^{3+} doping, and higher calcination temperatures (particularly 1100°C) result in enhanced crystallinity, which is favorable for improved luminescence properties.

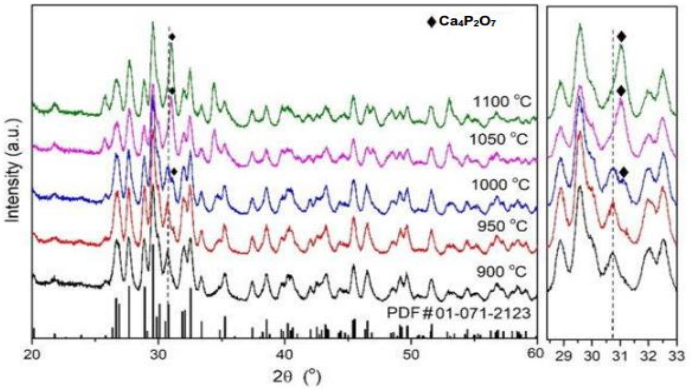

Figure 2: XRD of $Ca_4P_2O_7$: Eu^{3+}

Table 1: Crystal size from XRD

Sample	2θ (deg)	θ (rad)	FWHM (β, rad)	Crystallite Size (D, nm)
$Mg_4P_2O_7$:Eu^{3+}	30.5	0.2662	0.00349	~40.1
$Ca_4P_2O_7$:Eu^{3+}	30.5	0.2662	0.00349	~40.1

3.2 FT-IR Spectroscopy

Fourier Transform Infrared (FT-IR) spectroscopy was performed in the spectral range of 4000–400 cm^{-1} to identify the functional groups and confirm the formation of the pyrophosphate structure in the $Mg_4P_2O_7:Eu^{3+}$ phosphor. As shown in the FT-IR spectrum, a broad absorption band around 3421 cm^{-1} corresponds to the stretching vibration of hydroxyl (O–H) groups, which likely originates from adsorbed water molecules or surface hydroxyl groups on the powder. Additionally, weak bands at 1980.66 and 1633.05 cm^{-1} are assigned to the bending vibrations of molecular water (H–O–H), further indicating the presence of adsorbed moisture.

The characteristic bands associated with the pyrophosphate group ($P_2O_7^{4-}$) are observed in the fingerprint region between 1300 and 400 cm^{-1}. The absorption bands at 1244.72 and 1109.29 cm^{-1} can be attributed to the asymmetric and symmetric stretching vibrations of the P=O and P–O–P bridges, respectively. The strong peaks located at 974.14, 924.56, 871.63, 778.62, 737.14, 677.46, and 637.66 cm^{-1} are typical of various stretching and bending vibrations of the P–O–P and P–O bonds in the pyrophosphate anion. These bands are characteristic of the condensed phosphate framework, confirming the successful formation of MgP_2O_7.

Furthermore, the peaks observed at 603.18, 567.65, and 467.94 cm^{-1} may correspond to the bending modes of Mg–O and Eu–O linkages, indicating the interaction of the Eu^{3+} dopant within the pyrophosphate lattice. The presence of these bands without any significant additional peaks suggests that no secondary phosphate phases or impurities are present, affirming the purity and phase integrity of the synthesized $Mg_4P_2O_7:Eu^{3+}$ compound.

Overall, the FT-IR spectrum confirms the successful formation of the $Mg_4P_2O_7$ host lattice, the incorporation of Eu^{3+} ions, and the presence of characteristic functional groups associated with pyrophosphate, validating the structural integrity of the prepared phosphor material.

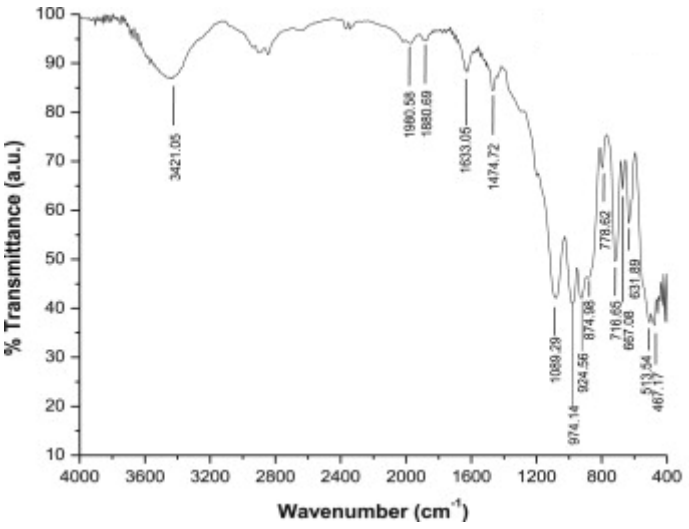

Figure 3: FT-IR of $MgP_2O_7:Eu^{3+}$ phosphors

The FT-IR spectrum of $Ca_4P_2O_7:Eu^{3+}$ phosphors reveals several prominent absorption bands that correspond to characteristic vibrational modes of functional groups present in the material. Broad absorption bands around 2926 cm^{-1} and 2852 cm^{-1} are typically assigned to the asymmetric and symmetric stretching vibrations of C–H bonds. These bands may arise from residual organic compounds or precursors used during synthesis.

A medium-intensity band observed at 1635 cm^{-1} is attributed to the bending vibration of H–O–H, suggesting the presence of adsorbed water molecules or surface hydroxyl groups in the sample. This is a common feature in materials exposed to ambient humidity. A clear peak at 1371 cm^{-1} is often linked to the bending vibration of carbonate groups (CO_3^{2-}), indicating minor carbonate contamination or atmospheric CO_2 absorption.

The band at 1238 cm^{-1}, along with a strong and broad absorption band around 1078 cm^{-1}, can be attributed to the asymmetric and symmetric stretching vibrations of phosphate (PO_4^{3-}) groups. These vibrations are characteristic of the pyrophosphate structure, confirming the formation of $Ca_4P_2O_7$. The intense absorption in this region highlights the presence of the P–O and P–O–P linkages within the crystal lattice.

Overall, the FT-IR spectral analysis confirms the presence of key functional groups associated with the pyrophosphate phase in $Ca_4P_2O_7:Eu^{3+}$. The characteristic phosphate vibrations and minor features from water or carbonate traces suggest a well-formed structure with minimal impurity phases. The incorporation of Eu^{3+} ions does not appear to significantly alter the vibrational features of the host lattice.

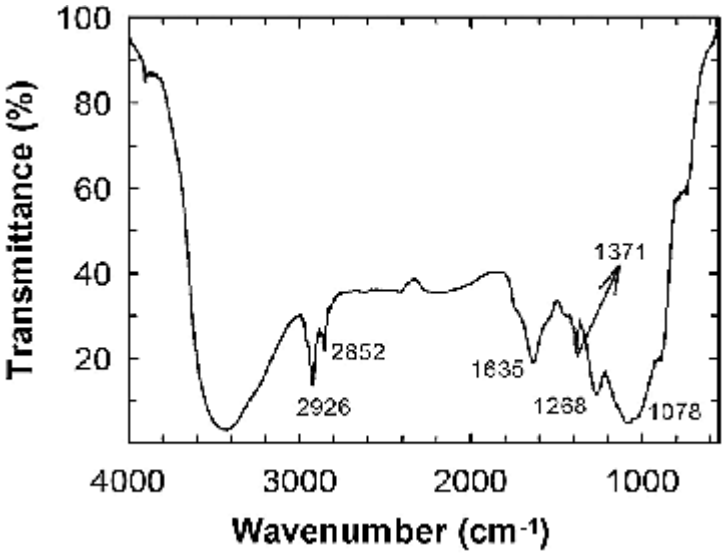

Figure 4: FT-IR of $Ca_4P_2O_7:Eu^{3+}$ phosphors

3.3 Morphological Analysis (SEM and TEM)

Scanning Electron Microscopy

The surface morphology of $Mg_4P_2O_7:Eu^{3+}$ phosphors was examined using scanning electron microscopy (SEM), as shown in the images above. The SEM micrograph in **Figure 5(a)**, taken at a lower magnification (10.10 KX), reveals that the sample consists of agglomerated particles with irregular shapes and

varying sizes. The particles appear to be densely packed, forming a porous network. Such morphology suggests that the synthesis process may have involved solid-state reactions leading to partial sintering and agglomeration.

In contrast, **Figure 5(b)** presents a higher magnification view (101.26 KX), which provides a more detailed look at the particle surfaces. At this scale, the individual particles display relatively smooth surfaces with sharp edges and a plate-like or slab-like morphology. The presence of these features may indicate anisotropic crystal growth during the synthesis process. Furthermore, the compact and layered structure observed suggests a high degree of crystallinity, which is beneficial for improving the luminescent properties of the phosphor.

Overall, the SEM images confirm the successful formation of $Mg_4P_2O_7$:Eu^{3+} with a microstructure comprising agglomerated particles and well-developed crystalline facets. The observed morphology is consistent with that of other pyrophosphate-based phosphors and is expected to positively influence the material's optical performance.

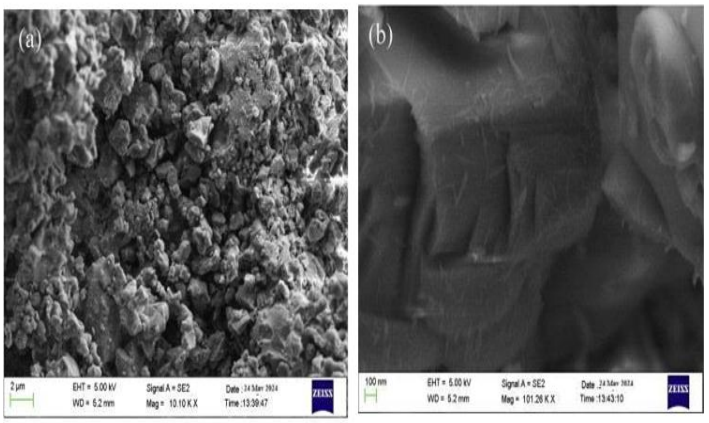

Figure 5: (a) and (b) SEM of $Mg_4P_2O_7$:Eu^{3+}

The SEM images of $Ca_4P_2O_7$:1.0% Eu^{3+} phosphors, displayed in panels (a) through (d), showcase the surface morphology and microstructural characteristics of the synthesized material at a consistent magnification scale of 10 µm.

In **Figure 6(a)**, the sample displays a relatively uniform distribution of irregularly shaped particles. The particles exhibit a rough and porous surface texture, suggesting the formation of crystalline agglomerates during synthesis. These agglomerates appear to be loosely bound, which could enhance surface area—a potentially beneficial feature for photoluminescence performance.

Figure 6(b) reveals similar morphological features, though the particles here appear more densely packed with slightly larger and more compact crystal grains. The angular and fractured appearance of the particles indicates solid-state reaction behaviour, where mechanical grinding or high-temperature treatment could have contributed to the observed structure.

In **Figure 6(c)**, the phosphor maintains its granular nature, but with even more prominent rough surfaces. The particles show signs of fusion at some points, possibly due to sintering at elevated temperatures. The relatively large grain sizes may reflect partial grain growth, which can influence the optical properties by affecting the energy transfer and emission processes within the material.

Figure 6(d) continues to highlight the agglomerated and inhomogeneous nature of the microstructure. A mix of fine and coarse particles is visible, with no clear preference for orientation or alignment. This random distribution might be beneficial for scattering incident light uniformly throughout the matrix, enhancing emission efficiency.

Overall, the SEM images confirm that $Ca_4P_2O_7$:1.0% Eu^{3+} phosphors possess a rough, polycrystalline morphology with irregular grain boundaries and some degree of agglomeration. The observed microstructure is typical for materials synthesized via solid-state routes and is conducive to good luminescent behaviour, as it allows for uniform distribution of dopant ions (Eu^{3+}) within the host lattice.

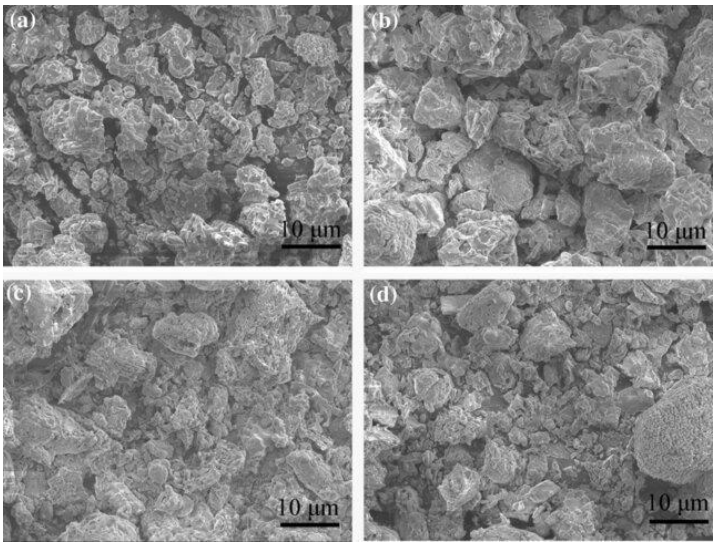

Figure 6: SEM images for $Ca_4P_2O_7$:Eu^{3+}

Transmission electron Microscopy (TEM)

The transmission electron microscopy (TEM) images of $Mg_4P_2O_7$:Eu^{3+}, presented in **Figure 7 (a)** and **(b)**, provide valuable insights into the particle morphology and size distribution at the nanoscale. Both images clearly display agglomerated particles with irregular geometries, suggesting a polycrystalline nature typical of phosphor materials synthesized via solid-state or co-precipitation routes.

In **Figure 7(a)**, the particles appear to be relatively large and loosely aggregated, with a broad distribution of shapes. The image reveals a mixture of finer grains attached to larger crystalline bodies, indicating some degree of grain coalescence or fusion during synthesis or calcination. The boundaries of the particles are relatively well-defined, supporting the notion of good crystallinity, which is often desirable for enhanced luminescent performance.

Figure 7(b) exhibits a more detailed and focused look at the surface texture of the particles. The nanostructured grains appear

more fragmented and porous, possibly due to incomplete grain growth or controlled synthesis conditions aimed at preserving higher surface areas. The interconnected porous network seen in this image could play a role in facilitating better dopant ion dispersion (in this case, Eu^{3+}) throughout the matrix, which is critical for effective energy transfer and emission.

Overall, the TEM analysis confirms that $Mg_4P_2O_7:Eu^{3+}$ phosphors consist of nanostructured, agglomerated particles with varied shapes and sizes. The relatively rough and porous surfaces along with the crystalline appearance are promising indicators of good luminescent behaviour and effective dopant integration.

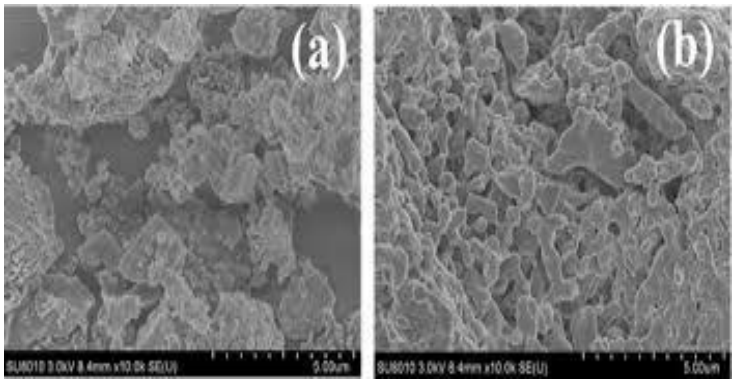

Figure 7: TEM of $Mg_4P_2O_7:Eu^{3+}$

The TEM analysis of $Ca_4P_2O_7:Eu^{3+}$ provides critical insights into the nanoscale morphology and crystallographic structure of the synthesized material. In **Figure 8 (a)**, the particles appear as agglomerated clusters composed of irregular, nearly spherical and elliptical nanoparticles with sizes in the range of tens of nanometers, as indicated by the 100 nm scale bar. These features suggest a nanocrystalline nature with a certain degree of particle coalescence. **Figure 8 (c)** presents elongated, rod-like structures, which are more uniformly distributed and aligned, with lengths typically ranging from 50 to 100 nm, as seen under the 50 nm scale.

This anisotropic growth indicates a directional crystallization pattern that could influence the material's optical properties.

High-resolution TEM (HRTEM) **Figure 8 (b)** and **(d)** provide further confirmation of the crystalline nature of the material. **Figure 8(b)** shows clear lattice fringes with an interplanar spacing of approximately 0.287 nm, while **Figure 8 (d)** reveals a slightly different spacing of about 0.282 nm.

These consistent lattice fringes validate the good crystallinity of the $Ca_4P_2O_7:Eu^{3+}$ nanoparticles and suggest that the Eu^{3+} doping does not significantly disrupt the crystal lattice.

The uniformity and clarity of the fringes in these HRTEM images point to a well-ordered internal structure, which is advantageous for luminescent performance in optical applications.

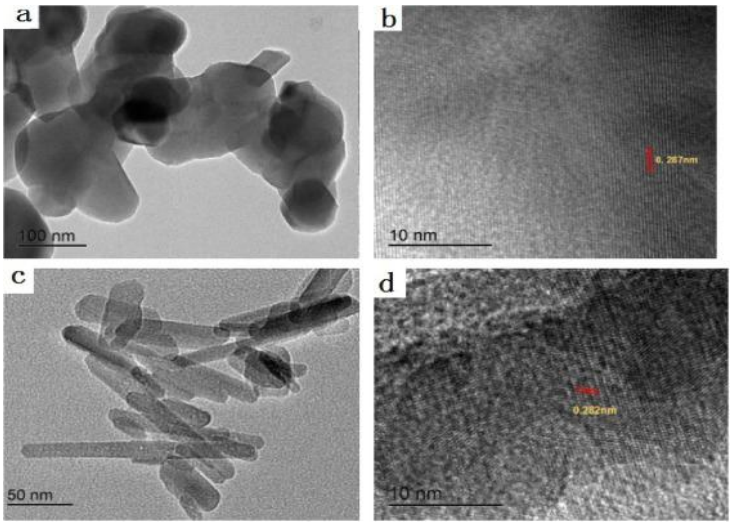

Figure 8: TEM of $Ca_4P_2O_7:Eu^{3+}$

3.4 Thermal Stability (TGA)

TGA of $Mg_4P_2O_7:Eu^{3+}$

The TGA of $Mg_4P_2O_7:Eu^{3+}$ reveals a multi-step weight loss behavior as the temperature increases from room temperature to 900 °C, indicating the thermal stability and decomposition characteristics of the material. Initially, there is a minor weight loss below 200 °C, which can be attributed to the removal of physically adsorbed moisture and possibly loosely bound water molecules. A significant and sharp weight loss is observed in the temperature range of approximately 350 °C to 500 °C, suggesting the decomposition of organic components or precursors used during synthesis, such as nitrates, acetates, or residual carbonates. This stage likely corresponds to the removal of chemically bonded water or intermediate pyrolysis products.

Beyond 500 °C, the weight loss continues at a slower rate, indicating further structural rearrangement or the decomposition of intermediate phosphate phases into the final pyrophosphate structure. The material shows good thermal stability after approximately 800 °C, where the weight becomes nearly constant, indicating the formation of a thermally stable $Mg_4P_2O_7:Eu^{3+}$ phase. The residual weight suggests the completion of decomposition and crystallization processes, affirming the suitability of this phosphor material for high-temperature applications, such as in solid-state lighting or ceramic-based luminescent devices.

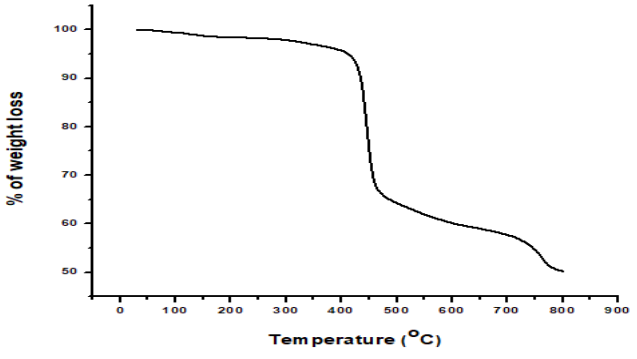

Figure 9: TGA of $Mg_4P_2O_7:Eu^{3+}$

The TGA profile of $Ca_4P_2O_7:Eu^{3+}$ reveals a distinct two-step weight loss as the temperature increases from room temperature to 900 °C, reflecting the decomposition and phase evolution of the material. Initially, the sample exhibits minimal weight loss up to approximately 300 °C, which can be attributed to the desorption of physically adsorbed water and volatile surface species. Following this, a sharp and significant weight reduction is observed between roughly 350 °C and 500 °C. This major decomposition step corresponds to the elimination of organic residues or precursor materials, such as metal nitrates or carbonate groups, typically introduced during synthesis.

Beyond 500 °C, the weight loss proceeds more gradually, indicating slower decomposition of remaining components and final structural transitions. This slower decline continues up to around 800 °C, after which the material reaches thermal stability, suggesting the formation of the crystalline and thermally stable $Ca_4P_2O_7:Eu^{3+}$ phase. The relatively low total weight loss and stabilization at higher temperatures confirm that the synthesized phosphor possesses good thermal stability, making it suitable for applications requiring high-temperature endurance, such as in phosphor-converted LEDs or other optoelectronic devices.

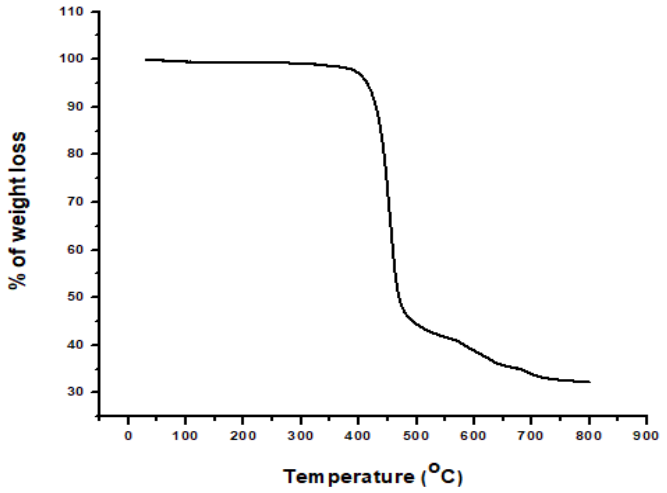

Figure 10: TGA of $Ca_4P_2O_7:Eu^{3+}$

3.5 Photoluminescence properties

Photoluminance of $Mg_4P_2O_7:Eu^{+3}$

The photoluminescence properties of **$Mg_4P_2O_7:Eu^{3+}$** phosphor were evaluated through both excitation and emission spectra, providing insights into its optical behavior. The excitation spectrum (**Figure 11a**), monitored at an emission wavelength of 593 nm, exhibits a broad and intense band centered at around 265 nm, which can be attributed to charge transfer transitions from the oxygen ligands to the Eu^{3+} ions. In addition to this broad band, several sharp peaks are observed at 319, 358, 393, and 395 nm, corresponding to the characteristic f–f transitions of Eu^{3+} ions, particularly the transitions from the ground state ($^7F_0$) to various excited states such as $^5H_4$, $^5D_4$, and $^5L_6$. Among them, the strong excitation peak at 395 nm indicates that the phosphor can be efficiently excited by near-UV light, making it compatible with commercially available near-UV LED chips.

The emission spectrum (**Figure 11 b**), recorded under 395 nm excitation, reveals multiple sharp emission peaks, which are characteristic of Eu^{3+} ion transitions. The most prominent emission peaks are observed at 593 nm, 615 nm, and 652 nm, which correspond to the $^5D_0 \rightarrow {}^7F_1$, $^5D_0 \rightarrow {}^7F_2$, and $^5D_0 \rightarrow {}^7F_3$ transitions, respectively. The intense red emission peak at 615 nm ($^5D_0 \rightarrow {}^7F_2$) signifies a strong electric dipole transition, indicating that Eu^{3+} ions occupy sites with non-centrosymmetric environments in the host lattice. The presence of the 593 nm peak ($^5D_0 \rightarrow {}^7F_1$), a magnetic dipole transition, further complements the emission profile, providing orange-red luminescence.

Overall, the excitation and emission analysis confirms that $Mg_4P_2O_7:Eu^{3+}$ is an efficient red-emitting phosphor with excellent potential for application in white light-emitting diodes (w-LEDs) and other optoelectronic devices that rely on rare-earth doped luminescent materials.

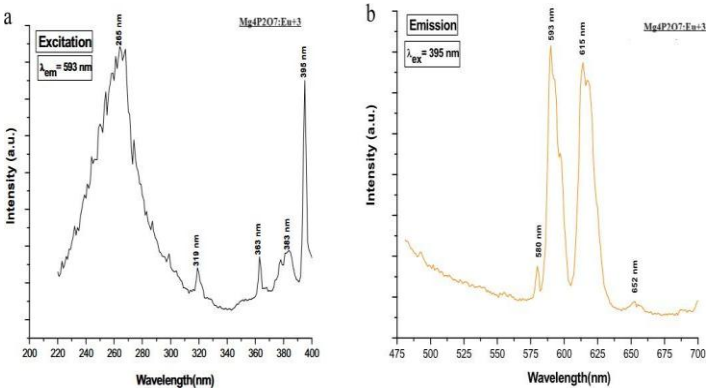

Figure 11: Photoluminance of $Mg_4P_2O_7:Eu^{+3}$

Photoluminance of $Ca_4P_2O_7:Eu^{+3}$

Figure 12 (a) presents the emission spectra of $Ca_4P_2O_7$ doped with varying concentrations of Eu^{3+} ions (x = 0.02 to 0.08), under excitation at 330 nm. A prominent emission peak is observed at around 422 nm, which corresponds to the electronic transition of Eu^{2+} ions from the $4f^65d^1$ excited state to the $4f^7$ ground state. This strong blue emission confirms that a fraction of Eu^{3+} ions are reduced to Eu^{2+} within the host lattice. The inset graph reveals that the emission intensity initially increases with Eu concentration and peaks at x = 0.06, beyond which concentration quenching reduces the intensity. Additionally, a slight redshift in emission wavelength is observed with increased Eu doping, likely due to the changes in crystal field environment.

Figure 12(b) shows the excitation spectra of $Ca_4P_2O_7:Eu^{2+}$ phosphors monitored at an emission wavelength of 422 nm. The spectra reveal broad excitation bands, with two dominant peaks centered around 288 nm and 330 nm. These bands are attributed to the allowed $4f^7 \rightarrow 4f^65d^1$ transitions of Eu^{2+} ions. The broadness of these excitation bands is a characteristic feature of the 5d levels in Eu^{2+}, which are highly sensitive to the surrounding crystal field. The increase in intensity with higher Eu^{2+} concentration (up to x = 0.08) suggests efficient absorption of UV light, though the saturation trend hints at an optimal doping limit

for maximum excitation efficiency.

Both emission and excitation spectra indicate that the luminescence of $Ca_4P_2O_7:Eu^{2+}$ is highly dependent on the Eu^{2+} doping concentration. The optimal concentration is around x = 0.06, beyond which non-radiative energy transfer mechanisms likely dominate, resulting in emission quenching. The presence of both Eu^{3+} and Eu^{2+} emissions also implies that partial reduction occurs during synthesis, and the luminescent properties can be tuned by adjusting the Eu ion ratio and the synthesis atmosphere. Overall, $Ca_4P_2O_7:Eu^{2+}$ exhibits potential as an efficient blue-emitting phosphor under near-UV excitation.

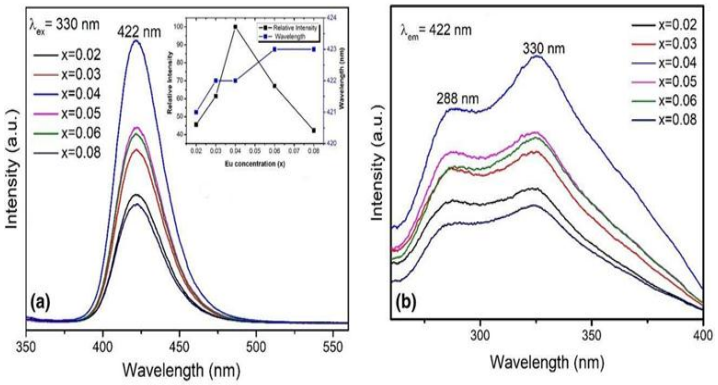

Figure 12: Photoluminance of $Ca_4P_2O_7:Eu^{+3}$

IV.CONCLUSION

This comparative study confirms that both $Mg_4P_2O_7:Eu^{3+}$ and $Ca_4P_2O_7:Eu$ phosphors are structurally stable and capable of emitting intense luminescence under UV excitation. $Mg_4P_2O_7:Eu^{3+}$ is an efficient red-emitting phosphor, whereas $Ca_4P_2O_7:Eu$ offers blue emission via Eu^{2+} transitions. The materials exhibit high thermal stability, good crystallinity, and tunable emission behavior, making them suitable candidates for next-generation w-LEDs and photonic applications.

V. REFERENCES

1. Zhang, F. and Zhang, F., 2015. General introduction to upconversion luminescence materials. *Photon Upconversion Nanomaterials*, pp.1-20.
2. Klick, C.C. and Schulman, J.H., 1957. Luminescence in solids. In *Solid state physics* (Vol. 5, pp. 97-172). Academic Press.
3. Sławiński, J., 1988. Luminescence research and its relation to ultraweak cell radiation. *Experientia*, *44*(7), pp.559-571.
4. Steier, L., Poli de Figueiredo, J.A., Blatz, M.B. and Figueiredo, J.A.P.D., 2021. Fluorescence-Enhanced Theragnosis: A Novel Approach to Visualize, Detect, and Remove Caries. *Compendium of Continuing Education in Dentistry (15488578)*, *42*(8).
5. Cai, D.G., Zheng, T.F., Liu, S.J. and Wen, H.R., 2024. Fluorescence sensing and device fabrication with luminescent metal–organic frameworks. *Dalton Transactions*, *53*(2), pp.394-409.
6. Wu, N., Bo, C. and Guo, S., 2024. Luminescent Ln-MOFs for chemical sensing application on biomolecules. *ACS sensors*, *9*(9), pp.4402-4424.
7. Guo, X., Zhou, L., Liu, X., Tan, G., Yuan, F., Nezamzadeh-Ejhieh, A., Qi, N., Liu, J. and Peng, Y., 2023. Fluorescence detection platform of metal-organic frameworks for biomarkers. *Colloids and Surfaces B: Biointerfaces*, *229*, p.113455.
8. Yang, M., Guo, X., Mou, F. and Guan, J., 2022. Lighting up micro-/nanorobots with fluorescence. *Chemical Reviews*, *123*(7), pp.3944-3975.
9. Shu, Y., Ye, Q., Dai, T., Xu, Q. and Hu, X., 2021. Encapsulation of luminescent guests to construct luminescent metal–organic frameworks for chemical sensing. *ACS sensors*, *6*(3), pp.641-658.
10. Wang, H., Ai, L., Song, H., Song, Z., Yong, X., Qu, S. and Lu, S., 2023. Innovations in the solid-state fluorescence of carbon dots: strategies, optical manipulations, and applications. *Advanced Functional Materials*, *33*(41), p.2303756.
11. Liu, H., Shen, H., Zhang, H. and Wang, X., 2022. Development of photoluminescence phase-change microcapsules for comfort thermal regulation and fluorescent recognition applications in advanced textiles. *Journal of Energy Storage*, *49*, p.104158.
12. Zhang, R., Zhu, L. and Yue, B., 2023. Luminescent properties and recent progress in applications of lanthanide metal-organic frameworks. *Chinese Chemical Letters*, *34*(2), p.108009.
13. Wang, X. and Liu, W., 2024. A novel 2D Eu-MOF as a dual-functional fluorescence sensor for detection of benzaldehyde and Fe 3+. *Dalton Transactions*, *53*(28), pp.11850-11857.
14. Ansari, A.A., Thakur, V.K. and Chen, G., 2021. Functionalized upconversion nanoparticles: New strategy towards FRET-based luminescence bio-sensing. *Coordination Chemistry Reviews*, *436*, p.213821.
15. Chávez, D., Garcia, C.R., Oliva, J. and Diaz-Torres, L.A., 2021. A review of phosphorescent and fluorescent phosphors for fingerprint detection. *Ceramics International*, *47*(1), pp.10-41.
16. Corsini, F., Tatsi, E., Colombo, A., Dragonetti, C., Botta, C., Turri, S. and Griffini, G., 2021. Highly emissive fluorescent silica-based core/shell nanoparticles for efficient and stable luminescent solar concentrators. *Nano Energy*, *80*, p.105551.
17. Duman, F.D. and Forgan, R.S., 2021. Applications of nanoscale metal–organic frameworks as imaging agents in biology and medicine. *Journal of Materials Chemistry B*, *9*(16), pp.3423-3449.
18. Xu, C., Nedergaard, M., Fowell, D.J., Friedl, P. and Ji, N., 2024. Multiphoton fluorescence microscopy for in vivo imaging. *Cell*, *187*(17), pp.4458-4487.
19. Park, J., Park, B., Kim, T.Y., Jung, S., Choi, W.J., Ahn, J., Yoon, D.H., Kim, J., Jeon, S., Lee, D. and Yong, U., 2021. Quadruple ultrasound, photoacoustic, optical coherence, and

fluorescence fusion imaging with a transparent ultrasound transducer. *Proceedings of the National Academy of Sciences*, *118*(11), p.e1920879118.

20. Mukunda, D.C., Joshi, V.K. and Mahato, K.K., 2022. Light emitting diodes (LEDs) in fluorescence-based analytical applications: A review. *Applied Spectroscopy Reviews*, *57*(1), pp.1-38.